ACS Energy LETTERS

http://pubs.acs.org/journal/aelccp

Improved Rate Capability for Dry Thick Electrodes through Finite Elements Method and Machine Learning Coupling

Mehdi Chouchane, Weiliang Yao, Ashley Cronk, Minghao Zhang,* and Ying Shirley Meng*

Cite This: *ACS Energy Lett.* 2024, 9, 1480−1486

Read Online

ACCESS | Metrics & More | Article Recommendations | Supporting Information

ABSTRACT: A coupled finite elements method (FEM) and machine learning (ML) workflow is presented to optimize the rate capability of thick positive electrodes (ca. 150 μm and 8 mAh/cm^2). An ML model is trained based on the geometrical observables of individual $LiNi_{0.8}Mn_{0.1}Co_{0.1}O_2$ particles and their average state of discharge (SOD) predicted from FEM modeling. This model not only bypasses lengthy FEM simulations but also provides deeper insights on the importance of pore tortuosity and the active particle size, identified as the limiting phenomenon during the discharge. Based on these findings, a bilayer configuration is proposed to tackle the identified limiting factors for the rate capability. The benefits of this structured electrode are validated through FEM by comparing its performance to a pristine monolayer electrode. Finally, experimental validation using dry processing demonstrates a 40% higher volumetric capacity of the bilayer electrode when compared to the previously reported thick NMC electrodes.

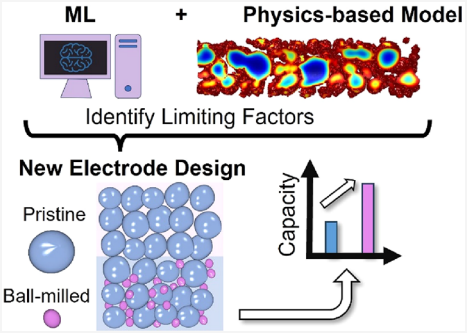

A promising route to reaching higher energy densities is increasing the thickness of the electrodes to maximize the loading of active materials. By increasing the active material volume within the electrode, larger amounts of energy can be stored, enabling electric vehicles (EVs) to travel longer distances on a single charge. However, thick electrodes are widely recognized for their inadequate rate capability,[1] leading to an even lengthier charging time for EVs compared to the current, already lengthy, duration. The main bottleneck hindering fast (dis)charging is still being debated in the scientific community.[2] Putting aside the mechanical challenges,[3,4] it can be attributed either to the limited electronic conductivity due to a tortuous carbon network[5] or to the poor wettability, tortuous pore phase, and length of the diffusion path of ions to reach the current collector which will lead to a sluggish ionic transport.[6,7] This Letter considers thick electrodes that are beyond the currently commercially available positive electrodes (ca. 100 μm).

Modeling can serve as a valuable tool for guiding experimental design and identifying limiting factors within a system.[8,9] 3-D digital twins have been used in the context of thick electrodes first by Danner et al. to highlight the importance of the connectivity of the electronically conductive network throughout all the thickness of the electrode.[9] Lu et al. quantified the heterogeneity within an electrode in terms of state of lithiation based on its thickness.[10] However, the use of computationally expensive 3-D finite elements method (FEM) simulations restricts the ability to thoroughly analyze a wide range of parameters and their individual impacts. Machine learning (ML) is a suitable approach to accelerate predictions, even for experimental inputs with, for instance, Severson et al.[11] who could accurately predict the cycle life (nominal capacity >80%) of a cell based on the first 100 cycles. Recently, Marcato et al.[12] employed ML coupled with FEM simulations to predict the spatial distribution of the state of discharge (SOD) in 3-D and discharge curves. Although this approach significantly reduces the time and resources required for accurate predictions, it still lacks deeper insights regarding the relationship between the SOD and the electrode's features. In the context of thick electrodes, only graphite electrodes have been studied, either through the optimization of the pore-channel design[13,14] or the prediction of the performance based on the manufacturing parameters.[15]

In this work, an ML model is trained using a data set of FEM simulations to predict the average state of lithiation at different depths of discharge for each $LiNi_{0.8}Mn_{0.1}Co_{0.1}O_2$ (NMC_{811}) particle. The novelty in this approach is to consider each

Received: January 19, 2024
Revised: March 5, 2024
Accepted: March 7, 2024

particle in the electrode as a data point instead of each simulation, which will considerably speed up obtaining a large enough representative data set (Scheme 1). Moreover, through

Scheme 1. Workflow of the Computational Approach Developed in This Work, from the Stochastic Generation of Electrodes, the Finite Elements Method (FEM), to the Training of the Machine-Learning (ML) Model Based on the State of Discharge (SOD) of Each Particle[a]

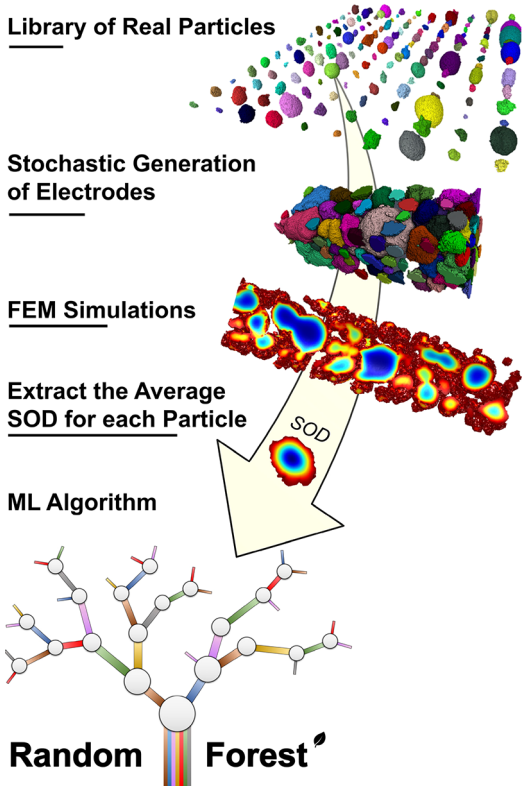

[a]For each step, the scale bar under the label represents 50 μm.

the implementation of Shapley additive explanation (SHAP) values,[16] the contribution of each parameter to the SOD is elucidated, thereby revealing the most prominent hindering phenomena. Based on these findings, a structured bilayer positive electrode design is proposed to enhance the rate capability. This design is first validated via an FEM simulation and subsequently verified experimentally, where the half-cells at current densities of 8 and 4 mA/cm^2 (1C and $C/2$, respectively) demonstrate a volumetric capacity surpassing that of any previously reported NMC thick electrodes at those discharge rates. The electrodes were manufactured using dry coating, which has been highlighted as an effective processing method to obtain mechanically robust and homogeneous thick electrodes.[17]

Machine-Learning Validation for Thick Electrode. The system modeled in this work is a 30 × 30 × 150 μm^3 electrode with 93 wt % of NMC_{811}, 5 wt % of vapor grown carbon fibers (VGCF), and 2 wt % of Poly(tetrafluoroethylene) binder (PTFE). The electrodes were stochastically generated using an in-house MATLAB code which is provided, as is all the code and the COMSOL Multiphysics template used to model a discharge of 1C (see the Supporting Information for details on the generation and Tables S1 and S2 for details on the model).

The limiting factor to the training of an effective ML model is usually obtaining a large enough amount of data. Here, only 10 FEM simulations with different stochastic electrodes were needed to build a satisfactory training data set. This was made possible since the ML model will predict an output for individual particles, and then in each FEM simulation, each NMC_{811} particle is a data point. To increase the understanding of the underlying limiting phenomena and go beyond the work of Marcato et al.,[12] the observables fed to the ML algorithm are geometrical features of the particles/electrodes. Namely, the volume of the NMC particle, its active surface area (surface in contact with the electrolyte), its position along the thickness of the electrode, the surface area in contact with CBD, and the tortuosity of the electrolyte from the separator plane to the particle plane (using TauFactor).[18] The output of the ML algorithm is the prediction of the average SOD for individual particles at different depth of discharge (DOD).

A random forest algorithm was trained with the as-described data set, and its predictions for a new data set are compared to the actual FEM simulation outputs in Figure 1A. In Figure 1A,

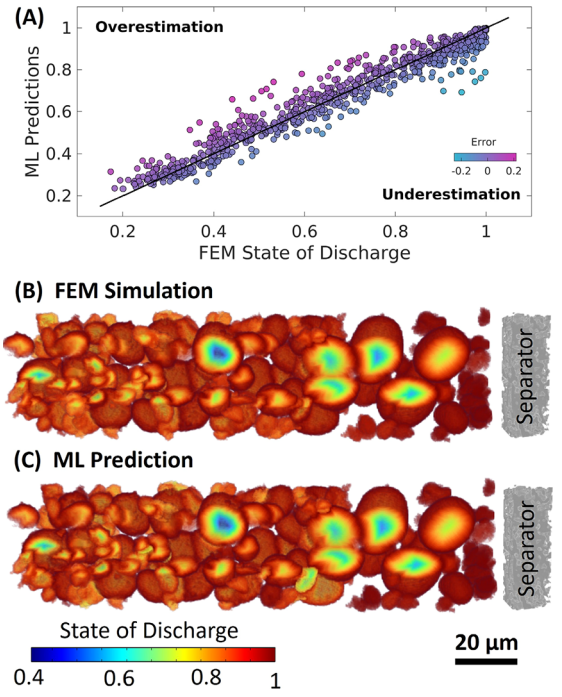

Figure 1. (A) Scatter plot of the ML-predicted values of the state of discharge of individual particles as a function of the values obtained through FEM simulations. The solid black line represents the region where the predictions are identical to the obtained values. 3D distribution of the state of discharge at the cutoff voltage (3 V) for (B) the FEM simulation and (C) the trained ML algorithm. The relative gradients representing state of discharge inside individual particles were assumed to be constant and equal to the average value of the relative gradients extracted from FEM simulations.

each point represents a particle at a given DOD. The greater the distance between the $x = y$ curve and a point, the greater the prediction error. Here, we can observe a satisfactory agreement between the actual values and the predictions, with an average error of 0.042 and an average relative error (the absolute error divided by the actual SOD value from FEM simulations) of 7.3%, thus validating the accuracy of our

https://doi.org/10.1021/acsenergylett.4c00203
ACS Energy Lett. 2024, 9, 1480−1486

trained model. An example of an electrode is provided in Figure 1B,C with the SOD at the end of discharge plotted in 3-D from an FEM simulation and the predictions from the ML algorithm. Since the ML algorithm can only predict the average value of the SOD, for both cases a uniform intraparticle gradient of concentration was assumed for plotting while keeping the proper average SOD predicted by both modeling methods. Only a few particles display a noticeable difference between the FEM simulation and the ML predictions. This is particularly impressive since each COMSOL simulation performed in this work required several hours to compute, while the prediction time for the ML workflow is 2 orders of magnitude lower (around 1 min).

The novelty of this workflow lies in the simplicity of setting it up, requiring only 10 FEM simulations and a fast-to-train random forest algorithm (under an hour in this case) to achieve such a high accuracy. Moreover, the use of geometrical observables of particles allows a deeper understanding of their contribution to the NMC utilization. This work paves the way toward a wider use of ML tools by proposing a quick workflow and by providing all the code and the COMSOL template necessary.

Limiting Factors for High-Rate Capability. ML algorithms usually suffer from the "black box" syndrome, where their predictions are accurate, but the users cannot unravel further insights on how each input parameter will impact the output. Explanatory artificial intelligence (XAI) aims to address this issue by providing techniques to have a better grasp at the thought process behind the ML predictions.[19] Among these techniques, the study of the Shapley additives explanation (SHAP) values has been on the rise in the battery field.[20,21] The strength of this approach is to identify for each input feature its impact on the SOD depending on its relative value, for instance, the impact a large or a small value of CBD contact would have on the predicted SOD. In essence, to determine SHAP values, sub-ML algorithms of all the combinations with a lower amount of input features will be trained. For each data point, the evolution of the prediction when introducing a new input feature in the ML model will be studied; see the Supporting Information for further explanations on SHAP.

Figure 2A displays the SHAP values for all the data point of the validation data set, and each feature is ranked from the most to the least impactful from top to bottom. How impactful a feature is can be seen from the range of its SHAP values, while the color gives the trend on how this feature has a positive or negative influence on the SOD. The ionic transport through the electrolyte tortuosity is the feature with the highest range of SHAP values, with low tortuosity inducing a better NMC_{811} utilization. Indeed, from Figure 2B the electrolyte tortuosity and the average SOD are plotted as a function of the distance from the current collector from ML predictions. Opposite trends can be observed, with the NMC_{811} particles being more utilized near the separator, while the tortuosity increases as we get closer to the current collector. This corroborates the impact of the tortuosity of the electrolyte on the particles' utilization as highlighted by Figure 2A. Regarding the volume of the NMC_{811} particles, it transpires that smaller particles will have a higher SOD than larger particles, which is in agreement with the current studies in the literature to optimize the particle size of active material.[22] Further investigations on the distribution of the SOD for NMC_{811} particles separated into 3 groups (Figure 2C) demonstrate that

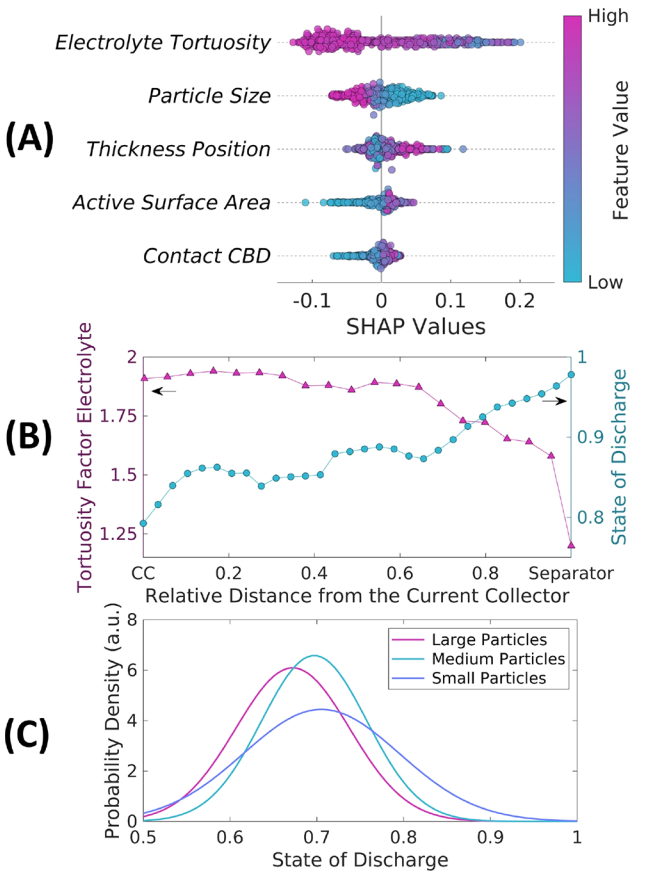

Figure 2. (A) Plot of the SHAP values extracted from the trained ML algorithm for the different features. Each point represents a data point of the data set used for verification, and the color code is a function of the relative value of each parameter. (B) The tortuosity factor in the electrolyte and CBD measured from the separator to different depths of the electrode and the average state of discharge (from ML) as a function of the distance from the current collector. The electrode was divided into subslices along the direction of the thickness, and the plotted SOD value is the average SOD value in each subslice. (C) Fitted normal distributions of the state of discharge of the NMC_{811} particles of the half of the electrode closer to the current collector (where differences are higher) divided into three groups based on the volume of NMC particles.

the peak of distribution for larger particles corresponds to a lower SOD than the other groups. Interestingly, the "small particles" group has a wider distribution of SOD than the others, which can be explained by the difficulty to connect all the smaller particles to the carbon network. Indeed, Figure S1 sheds light on the lower current density at the surface of the "small particles" compared with the larger NMC_{811} particles.

The third most impactful feature is the thickness position of the particle (0 μm being the current collector), with particles closer to the separator experiencing a higher lithiation in comparison to the particles close to the current collector. This phenomenon can also be attributed to systems limited by the ionic transport, as mentioned in the literature.[8,10] Lastly, the active material surface and the contact with the carbon network both follow the same trend: the higher the feature value, the higher the SOD. Here, the contact with the CBD phase has a minor impact on the SOD because the fiber morphology and the homogeneous distribution of the VGCF

https://doi.org/10.1021/acsenergylett.4c00203
ACS Energy Lett. 2024, 9, 1480−1486

enable an efficient electronic network for all the NMC_{811} particles.

Structured Bilayer Electrode. Due to the coupled FEM-ML workflow, the most impactful features have been identified in the context of fast discharge for thick NMC_{811} electrodes, with the tortuosity of the pore network at the top of the list. While there has been a great deal of research on how to decrease tortuosity in thick electrodes using laser structuring,[23] its use can lead to a deterioration of the mechanical integrity of the electrode,[24] and its scalability and practical use at an industrial scale are still under development.[25] Therefore, this work will focus on the second most impactful feature for improving the electrochemical performance, namely, the volume of the NMC_{811} particles. Reducing the size of the particle will in turn increase the specific active surface area, which is beneficial to the NMC_{811} utilization according to the SHAP values. Also, in Figure 2B we observe a poor utilization of the NMC_{811} in the left half of the electrode, i.e., the half closer to the current collector. These observations motivated the suggested bilayer design, where the right layer, i.e., the one close to the separator, will remain unchanged, but the left half will consist of a mix of intact (75 wt %) and ball-milled (25 wt %) NMC_{811} particles. This ratio was chosen based on the quickly degrading mechanical properties of the film with higher ball-milled particle content. The added ball-milled particles with a lower volume and higher specific active surface area should help in achieving a higher utilization. Also, using the dry process, the layer with a mix of NMC_{811} would achieve a higher degree of compaction during the rolling step with a higher number of ball-milled particles, increasing the tortuosity of the pore network and hindering its performance. Shodiev et al.[26] and Hamedi et al.[27] have shown that having a more porous layer close to the separator and denser layer close to the current collector will have a positive impact on the performance. Hence, the choice was to put the mixed NMC_{811} layer close to the current collector. Structured electrodes have already been reported in the literature either through modeling studies[26,28] or investigated experimentally through slurry processed electrodes.[29,30] However, the slurry method can lead to inhomogeneous distribution of lighter components (carbon, binder) during the drying step, leading to weak mechanical properties,[31,32] especially for thick electrodes. Moreover, the bilayer electrode requires 2 different steps of slurry coating and drying, which is not cost/energy efficient. Whereas for dry coating, stacking two different films and calendaring them together suffices to yield a bilayer electrode, yet none have been reported in the literature to the authors' knowledge. Only the company Maxwell has reported a patent with a hybrid bilayer electrode made of one slurry-casted layer and one dry coated layer.[33]

To validate the benefit of this design, 1C discharge simulation comparison was performed between a pristine electrode and a bilayer electrode, both sharing the same top layer. The left layer of the bilayer electrode consisted of 75 wt % of pristine particles and 25 wt % of the same particles but shrunk by a factor of 6. Due to the associated computational cost, it was impossible to use primary particles instead of secondary ones for the ball-milled particles to mimic the experiment (see Figure S2). The 3-D distribution of the SOD at the end of discharge is represented for the pristine and bilayer electrodes, respectively, in Figure 3A,B. Figure 3C offers a quantitative comparison of the average SOD along the thicknesses of both electrodes. Regarding the top layer, the two

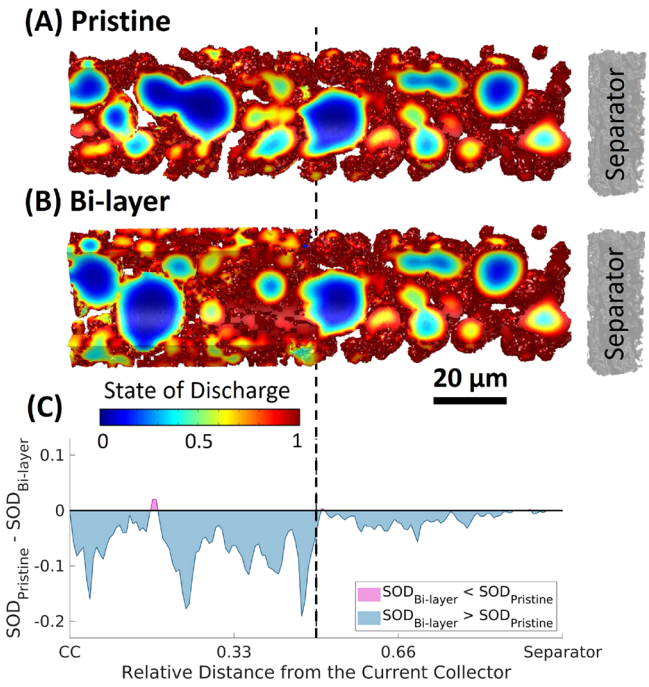

Figure 3. Modeling validation of the structured bilayer electrode design. Simulated 3-D distribution of the state of discharge at the end of a 1C discharge for the (A) pristine and (B) bilayer cases. Both electrodes share the same right half, only the left half is different. (C) Difference in the average state of discharge as a function of the distance from the current collector between the pristine layer (A) and bilayer (B).

electrodes share a similar NMC_{811} utilization, but there is a significant improvement at the left layer of the bilayer design. The bilayer electrode achieves a discharge capacity 11% superior to the pristine one at 8 mA/cm^2 (1C), mostly due to a higher utilization of the left layer thanks to the new bilayer architecture. The opposite configuration with the mixed NMC_{811} layer being near the separator has also been investigated through modeling and experiments in Figures S3 and S4, displaying stronger gradients and a decay in performance.

Experimental Validation for the Bilayer Thick Electrode. To prove the capability of this modeling workflow, 3 coin cells were fabricated for the pristine and bilayer electrodes (both 8 mAh/cm^2), which were paired with lithium foils as the counter electrode (see the Supporting Information for further manufacturing details).

Figure 4A shows the morphology of a bilayer electrode in the case of a bottom layer with twice the amount of ball-milled particles and binder to enable a robust film (93:3:4 wt % of NMC_{811}:VGCF:PTFE). The volume of ball-milled particles has been increased to enhance the visual difference between the two layers, and scanning electron microscopy images of pristine and standard bilayer electrodes are available in Figure S5. While we do observe a larger number of intact secondary NMC_{811} particles at the top and a larger number of primary particles at the bottom, ball-milled particles can still be found even close to the separator, i.e., the pristine layer. This could be induced by the calendaring process; indeed, NMC_{811} is known to be prone to cracking, especially the region close to the separator/calendaring roll.[34]

The rate tests results are summarized in Figure 4B, and the discharge curves are presented in Figure 4C. Similar discharge

https://doi.org/10.1021/acsenergylett.4c00203
ACS Energy Lett. 2024, 9, 1480−1486

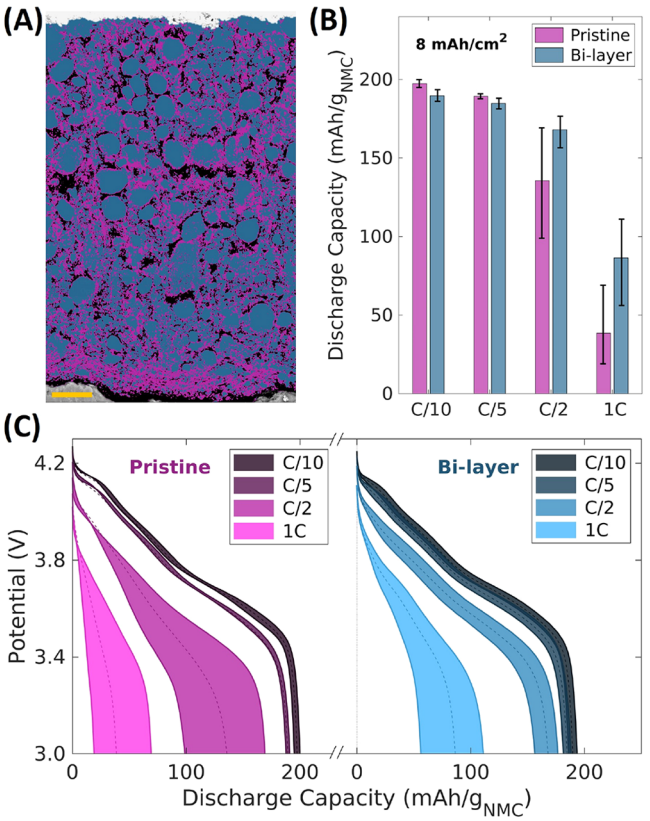

Figure 4. (A) Scanning electron microscopy image of a bilayer electrode with twice the amount of ball-milled NMC_{811} and PTFE in the bottom layer. The NMC_{811} is represented in blue, the VGCF +PTFE in purple, the current collector in gray, and the pores in black. The image has been segmented based on the gray levels in MATLAB. The scale bar represents 15 μm. (B) Discharge rate comparison between the pristine and bilayer cases in coin cells with an areal loading close to ca. 8 mAh/cm^2 and a constant charge at C/5. The bars represent the average value, and the error-bars represents the maximal and minimal values. (C) Discharge curves for the pristine and bilayer cases at different discharge rates. For each rate, the shaded area is delimited by the discharge curves of the half-cells with the largest and smallest discharge capacities, and the dashed line represents the average discharge curve of all cells.

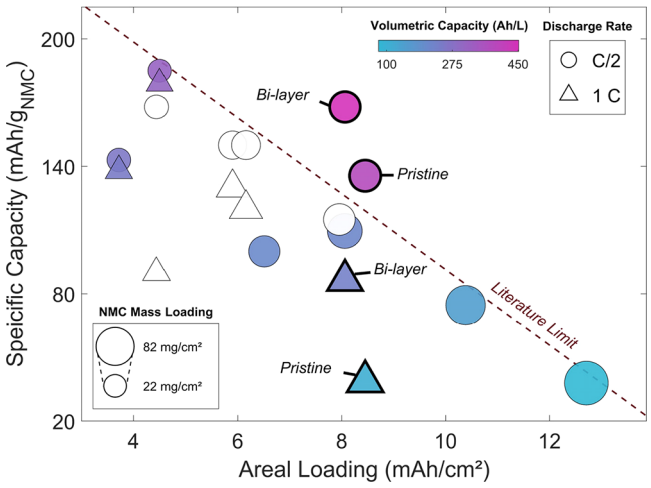

Figure 5. Literature review of the discharge capacity of thick NMC electrodes at high rates as a function of the areal loading and the volumetric capacity.[1,30,35−39] For the bilayer and pristine cases presented in this work, the average coin cells results are represented with thicker edges. The size of the symbols is proportional to the NMC mass loading, and the color white represents data points for which the volumetric capacity could not be calculated. The volumetric capacity was determined as the ratio between the actual areal discharge capacity (Ah/m^2) times and the electrode thickness (m). See Table S3 for the complete summary of the data used in this plot.

capacities are obtained at low rate until the $C/2$ threshold where the bilayer outperforms the pristine electrode. The bilayer half-cells achieve an average discharge capacity at a current density of 8 mA/cm^2 (1C) of 86 mAh/g_{NMC} and an average of 168 mAh/g_{NMC} at 4 mA/cm^2 (C/2), respectively around 125% and 25% higher than the pristine coin cells (38 mAh/g_{NMC} at 8 mA/cm^2 and 135 mAh/g_{NMC} at 4 mA/cm^2). The dispersion of values at a given rate is negligible at low rates (range of ca. 7 mAh/g_{NMC} at C/10 for the bilayer) but significantly increases at higher rates (range of ca. 54 mAh/g_{NMC} at 1C for the bilayer) as one could have expected. Such variations are inherent to the manual manufacturing of thick electrodes through dry processing.

These performances are particularly impressive when compared to the reported thick NMC electrode discharge capacities for the same rates. Figure 5 highlights how this work's results stand out from the literature in terms of discharge capacities for such a high loading. However, to sustain a satisfactory cycling life for the bilayer electrode, surface coating of the NMC_{811} is crucial to avoid accentuated side reactions due to the increased surface area.[22] While this study uses a constant charge rate during the discharge rate tests, which can boost the capacity compared to a symmetric rate test, it is noteworthy that most of the data points reported in Figure 5 are obtained by using further electrode modification (laser structuring, for instance). Another significant difference is the volumetric capacity achieved by the bilayer coin cells (ca. 450 Ah/L) which is almost twice as much as the other electrodes. Such an impressive volumetric capacity stems from the high discharge capacity at such a high loading, but also from the low porosity achieved by the dry coating method (ca. 30%), significantly lower than the standard porosity for thick electrodes, usually over 40%. The dry processing combined with the bilayer design presented here is promising because it yields both a high volumetric capacity at the electrode level and a high gravimetric capacity at the pack level at high rates.

In this work, an ML model has been trained using a limited number of lengthy FEM simulations and could yield dynamic SOD predictions for thick NMC_{811} electrodes with only 7.3% relative error. This unique FEM-ML coupling workflow draws its strength from having each particle in the electrode as a data point instead of each FEM simulation, significantly cutting down the required FEM simulations to build a large enough data set to train an ML model. The latter has a computation time 2 orders of magnitude lower than the FEM, allowing wide screenings of parameters which are too costly with FEM.

Subsequently, a more in-depth understanding of the limiting phenomena during the discharge has been evidenced using XAI through the study of SHAP values. The ionic transport and the morphology of the NMC_{811} particles were identified as the most impactful parameters during the lithiation of the positive electrode. The methodology of this work is promising and could be applied to a number of different systems to gain insights and address bottlenecks in battery fields. To promote the implementation of this approach, all the computational files

https://doi.org/10.1021/acsenergylett.4c00203
ACS Energy Lett. 2024, 9, 1480−1486

necessary to reproduce the workflow are provided to the community in the Supporting Information.

Based on those insights, a structured bilayer electrode with a layer close to the current collector consisting of a mix of pristine and ball-milled NMC_{811} was implemented. Its ability to improve the performance at rates as high as 8 mA/cm^2 was first investigated through modeling and then further verified through experimental validation. The bilayer electrodes displayed the highest volumetric capacity (450 Ah/L) in comparison to any reported thick NMC electrodes at such *C*-rates, twice as much as an electrode with a similar loading and discharge rate. The impressive performance with dense, thick electrodes and the simplicity of the manufacturing process to obtain bilayer dry electrodes is promising for its scalability at the industrial level.

■ ASSOCIATED CONTENT

Data Availability Statement

All the MATLAB/Python codes and the COMSOL template are available at https://github.com/LESCOpenAccess/Codes-and-Data.

Supporting Information

The Supporting Information is available free of charge at https://pubs.acs.org/doi/10.1021/acsenergylett.4c00203.

Additional experimental section, containing details on the electrode fabrication, coin cell cycling, powder imaging, stochastic generation of electrodes, FEM simulations, and ML model; additional figures and tables with the modeling equations and parameters mentioned in the text (PDF)

■ AUTHOR INFORMATION

Corresponding Authors

Minghao Zhang − *Department of NanoEngineering, University of California San Diego, La Jolla, California 92093, United States*; Email: miz016@eng.ucsd.edu

Ying Shirley Meng − *Pritzker School of Molecular Engineering, University of Chicago, Chicago, Illinois 60637, United States; Department of NanoEngineering, University of California San Diego, La Jolla, California 92093, United States*; orcid.org/0000-0001-8936-8845; Email: shirleymeng@uchicago.edu

Authors

Mehdi Chouchane − *Pritzker School of Molecular Engineering, University of Chicago, Chicago, Illinois 60637, United States*

Weiliang Yao − *Materials Science and Engineering, University of California San Diego, La Jolla, California 92093, United States*

Ashley Cronk − *Materials Science and Engineering, University of California San Diego, La Jolla, California 92093, United States*; orcid.org/0000-0001-6147-4662

Complete contact information is available at: https://pubs.acs.org/10.1021/acsenergylett.4c00203

Notes

The authors declare no competing financial interest.

■ ACKNOWLEDGMENTS

The authors are grateful to LG Chem for providing the NMC_{811} powder and to Chemours for providing the PTFE powder used in this study. The authors acknowledge C. Hamill 407 at the University of Chicago for server network administration. The FIB-SEM measurements in this work were performed in part at the San Diego Nanotechnology Infrastructure (SDNI) of UCSD, a member of the National Nanotechnology Coordinated Infrastructure, which is supported by the National Science Foundation (Grant ECCS-1542148). The authors thank the University of Chicago−France program (FACCTS, 2023) for its financial support.

■ REFERENCES

(1) Zheng, H.; Li, J.; Song, X.; Liu, G.; Battaglia, V. S. A Comprehensive Understanding of Electrode Thickness Effects on the Electrochemical Performances of Li-Ion Battery Cathodes. *Electrochim. Acta* **2012**, *71*, 258−265.

(2) Zhang, X.; Ju, Z.; Zhu, Y.; Takeuchi, K. J.; Takeuchi, E. S.; Marschilok, A. C.; Yu, G. Multiscale Understanding and Architecture Design of High Energy/Power Lithium-Ion Battery Electrodes. *Adv. Energy Mater.* **2021**, *11* (2), 2000808.

(3) Chiu, R. C.; Garino, T. J.; Cima, M. J. Drying of Granular Ceramic Films: I, Effect of Processing Variables on Cracking Behavior. *J. Am. Ceram. Soc.* **1993**, *76* (9), 2257−2264.

(4) Singh, K. B.; Tirumkudulu, M. S. Cracking in Drying Colloidal Films. *Phys. Rev. Lett.* **2007**, *98* (21), 218302.

(5) Lee, B.-S.; Wu, Z.; Petrova, V.; Xing, X.; Lim, H.-D.; Liu, H.; Liu, P. Analysis of Rate-Limiting Factors in Thick Electrodes for Electric Vehicle Applications. *J. Electrochem. Soc.* **2018**, *165* (3), A525.

(6) Zhang, X.; Zhu, Y.; Bruck, A. M.; Housel, L. M.; Wang, L.; Quilty, C. D.; Takeuchi, K. J.; Takeuchi, E. S.; Marschilok, A. C.; Yu, G. Understanding Aggregation Hindered Li-Ion Transport in Transition Metal Oxide at Mesoscale. *Energy Storage Materials* **2019**, *19*, 439−445.

(7) Kuang, Y.; Chen, C.; Kirsch, D.; Hu, L. Thick Electrode Batteries: Principles, Opportunities, and Challenges. *Adv. Energy Mater.* **2019**, *9* (33), 1901457.

(8) Chouchane, M.; Franco, A. A. Deconvoluting the Impacts of the Active Material Skeleton and the Inactive Phase Morphology on the Performance of Lithium Ion Battery Electrodes. *Energy Storage Materials* **2022**, *47*, 649−655.

(9) Danner, T.; Singh, M.; Hein, S.; Kaiser, J.; Hahn, H.; Latz, A. Thick Electrodes for Li-Ion Batteries: A Model Based Analysis. *J. Power Sources* **2016**, *334*, 191−201.

(10) Lu, X.; Bertei, A.; Finegan, D. P.; Tan, C.; Daemi, S. R.; Weaving, J. S.; O'Regan, K. B.; Heenan, T. M. M.; Hinds, G.; Kendrick, E.; Brett, D. J. L.; Shearing, P. R. 3D Microstructure Design of Lithium-Ion Battery Electrodes Assisted by X-Ray Nano-Computed Tomography and Modelling. *Nat. Commun.* **2020**, *11* (1), 2079.

(11) Severson, K. A.; Attia, P. M.; Jin, N.; Perkins, N.; Jiang, B.; Yang, Z.; Chen, M. H.; Aykol, M.; Herring, P. K.; Fraggedakis, D.; Bazant, M. Z.; Harris, S. J.; Chueh, W. C.; Braatz, R. D. Data-Driven Prediction of Battery Cycle Life before Capacity Degradation. *Nat. Energy* **2019**, *4* (5), 383−391.

(12) Marcato, A.; Santos, J. E.; Liu, C.; Boccardo, G.; Marchisio, D.; Franco, A. A. Modeling the 4D Discharge of Lithium-Ion Batteries with a Multiscale Time-Dependent Deep Learning Framework. *Energy Storage Materials* **2023**, *63*, 102927.

(13) Goel, V.; Chen, K.-H.; Dasgupta, N. P.; Thornton, K. Optimization of Laser-Patterned Electrode Architectures for Fast Charging of Li-Ion Batteries Using Simulations Parameterized by Machine Learning. *Energy Storage Materials* **2023**, *57*, 44−58.

(14) Gao, T.; Lu, W. Physical Model and Machine Learning Enabled Electrolyte Channel Design for Fast Charging. *J. Electrochem. Soc.* **2020**, *167* (11), 110519.

(15) Drakopoulos, S. X.; Gholamipour-Shirazi, A.; MacDonald, P.; Parini, R. C.; Reynolds, C. D.; Burnett, D. L.; Pye, B.; O'Regan, K. B.; Wang, G.; Whitehead, T. M.; Conduit, G. J.; Cazacu, A.; Kendrick, E. Formulation and Manufacturing Optimization of Lithium-Ion Graph-

ite-Based Electrodes via Machine Learning. *Cell Reports Physical Science* **2021**, *2* (12), 100683.
(16) Lundberg, S. M.; Lee, S.-I. A Unified Approach to Interpreting Model Predictions. In *Advances in Neural Information Processing Systems*; Curran Associates, Inc., 2017; Vol. *30*.
(17) Yao, W.; Chouchane, M.; Li, W.; Bai, S.; Liu, Z.; Li, L.; Chen, A. X.; Sayahpour, B.; Shimizu, R.; Raghavendran, G.; Schroeder, M. A.; Chen, Y.-T.; Tan, D. H. S.; Sreenarayanan, B.; Waters, C. K.; Sichler, A.; Gould, B.; Kountz, D. J.; Lipomi, D. J.; Zhang, M.; Meng, Y. S. A 5 V-Class Cobalt-Free Battery Cathode with High Loading Enabled by Dry Coating. *Energy Environ. Sci.* **2023**, *16* (4), 1620−1630.
(18) Cooper, S. J.; Bertei, A.; Shearing, P. R.; Kilner, J. A.; Brandon, N. P. TauFactor: An Open-Source Application for Calculating Tortuosity Factors from Tomographic Data. *SoftwareX* **2016**, *5*, 203−210.
(19) Gilpin, L. H.; Bau, D.; Yuan, B. Z.; Bajwa, A.; Specter, M.; Kagal, L. Explaining Explanations: An Overview of Interpretability of Machine Learning. In *2018 IEEE 5th International Conference on Data Science and Advanced Analytics (DSAA)*; IEEE: Turin, Italy, 2018; pp 80−89. DOI: 10.1109/DSAA.2018.00018.
(20) Nair, P.; Vakharia, V.; Borade, H.; Shah, M.; Wankhede, V. Predicting Li-Ion Battery Remaining Useful Life: An XDFM-Driven Approach with Explainable AI. *Energies* **2023**, *16* (15), 5725.
(21) Lee, G.; Kim, J.; Lee, C. State-of-Health Estimation of Li-Ion Batteries in the Early Phases of Qualification Tests: An Interpretable Machine Learning Approach. *Expert Systems with Applications* **2022**, *197*, 116817.
(22) Zhang, J.; Qiao, J.; Sun, K.; Wang, Z. Balancing Particle Properties for Practical Lithium-Ion Batteries. *Particuology* **2022**, *61*, 18−29.
(23) Pfleging, W. A. Review of Laser Electrode Processing for Development and Manufacturing of Lithium-Ion Batteries. *Nanophotonics* **2018**, *7* (3), 549−573.
(24) Hille, L.; Noecker, M. P.; Ko, B.; Kriegler, J.; Keilhofer, J.; Stock, S.; Zaeh, M. F. Integration of Laser Structuring into the Electrode Manufacturing Process Chain for Lithium-Ion Batteries. *J. Power Sources* **2023**, *556*, 232478.
(25) Pfleging, W. Recent Progress in Laser Texturing of Battery Materials: A Review of Tuning Electrochemical Performances, Related Material Development, and Prospects for Large-Scale Manufacturing. *Int. J. Extrem. Manuf.* **2021**, *3* (1), 012002.
(26) Shodiev, A.; Chouchane, M.; Gaberscek, M.; Arcelus, O.; Xu, J.; Oularbi, H.; Yu, J.; Li, J.; Morcrette, M.; Franco, A. A. Deconvoluting the Benefits of Porosity Distribution in Layered Electrodes on the Electrochemical Performance of Li-Ion Batteries. *Energy Storage Materials* **2022**, *47*, 462−471.
(27) Hamedi, A.-S.; Yao, A.; Martin, R.; Roig, R.; Valadez, M. R.; Pile, D.; Shellikeri, A.; Liu, B.; Wheeler, D. R. Multi-Layer Anodes for High-Current Applications. *Electrochim. Acta* **2023**, *439*, 141649.
(28) Lu, X.; Zhang, X.; Tan, C.; Heenan, T. M. M.; Lagnoni, M.; O'Regan, K.; Daemi, S.; Bertei, A.; Jones, H. G.; Hinds, G.; Park, J.; Kendrick, E.; Brett, D. J. L.; Shearing, P. R. Multi-Length Scale Microstructural Design of Lithium-Ion Battery Electrodes for Improved Discharge Rate Performance. *Energy Environ. Sci.* **2021**, *14* (11), 5929−5946.
(29) Chowdhury, R.; Zhao, Y.; Xia, Y.; Ouyang, M.; Brandon, N.; Banerjee, A. Revisiting the Promise of Bi-Layer Graded Cathodes for Improved Li-Ion Battery Performance. *Sustainable Energy & Fuels* **2021**, *5* (20), 5193−5204.
(30) Song, Z.; Zhu, P.; Pfleging, W.; Sun, J. Electrochemical Performance of Thick-Film Li(Ni0.6Mn0.2Co0.2)O2 Cathode with Hierarchic Structures and Laser Ablation. *Nanomaterials* **2021**, *11* (11), 2962.
(31) Klemens, J.; Schneider, L.; Herbst, E. C.; Bohn, N.; Müller, M.; Bauer, W.; Scharfer, P.; Schabel, W. Drying of NCM Cathode Electrodes with Porous, Nanostructured Particles Versus Compact Solid Particles: Comparative Study of Binder Migration as a Function of Drying Conditions. *Energy Technology* **2022**, *10* (4), 2100985.
(32) Font, F.; Protas, B.; Richardson, G.; Foster, J. M. Binder Migration during Drying of Lithium-Ion Battery Electrodes: Modelling and Comparison to Experiment. *J. Power Sources* **2018**, *393*, 177−185.
(33) Shin, J. H.; Duong, H. M.; Acevedo, A. M. G. *Compositions and Methods for Multilayer Dry Coated and Wet Cast Film Hybrid Electrode Films*. US 20200313175 A1. October 1, 2020. https://patents.google.com/patent/US20200313175A1/ewebn (accessed 2024-02-26).
(34) Heenan, T. M. M.; Wade, A.; Tan, C.; Parker, J. E.; Matras, D.; Leach, A. S.; Robinson, J. B.; Llewellyn, A.; Dimitrijevic, A.; Jervis, R.; Quinn, P. D.; Brett, D. J. L.; Shearing, P. R. Identifying the Origins of Microstructural Defects Such as Cracking within Ni-Rich NMC811 Cathode Particles for Lithium-Ion Batteries. *Adv. Energy Mater.* **2020**, *10* (47), 2002655.
(35) Singh, M.; Kaiser, J.; Hahn, H. A Systematic Study of Thick Electrodes for High Energy Lithium Ion Batteries. *J. Electroanal. Chem.* **2016**, *782*, 245−249.
(36) Singh, M.; Kaiser, J.; Hahn, H. Effect of Porosity on the Thick Electrodes for High Energy Density Lithium Ion Batteries for Stationary Applications. *Batteries* **2016**, *2* (4), 35.
(37) Du, Z.; Rollag, K. M.; Li, J.; An, S. J.; Wood, M.; Sheng, Y.; Mukherjee, P. P.; Daniel, C.; Wood, D. L. Enabling Aqueous Processing for Crack-Free Thick Electrodes. *J. Power Sources* **2017**, *354*, 200−206.
(38) Hu, J.; Wu, B.; Cao, X.; Bi, Y.; Chae, S.; Niu, C.; Xiao, B.; Tao, J.; Zhang, J.; Xiao, J. Evolution of the Rate-Limiting Step: From Thin Film to Thick Ni-Rich Cathodes. *J. Power Sources* **2020**, *454*, 227966.
(39) Park, S.-H.; King, P. J.; Tian, R.; Boland, C. S.; Coelho, J.; Zhang, C.; McBean, P.; McEvoy, N.; Kremer, M. P.; Daly, D.; Coleman, J. N.; Nicolosi, V. High Areal Capacity Battery Electrodes Enabled by Segregated Nanotube Networks. *Nat. Energy* **2019**, *4* (7), 560−567.